PALLADIUM COATED EDGE-EMITTING LASERS FOR HYDROGEN SENSING APPLICATIONS

BY

BENJAMIN GEORGE GRIFFIN

THESIS

Submitted in partial fulfillment of the requirements
for the degree of Master of Science in Electrical and Computer Engineering
in the Graduate College of the
University of Illinois at Urbana-Champaign, 2010

Urbana, Illinois

Adviser:

Assistant Professor Lynford L. Goddard

Abstract

As gas prices continue to rise and fossil fuels pollute our environment, various alternative fuel sources are being actively pursued. Hydrogen shows considerable promise due to its virtually unlimited supply, energy conversion efficiency, and neutral impact on the environment. However, due to the flammability of hydrogen gas in concentrations as low as 4%, reliable sensors capable of detecting small concentrations of hydrogen with quick response times are a necessity.

A novel type of hydrogen sensor utilizing a thin film of palladium deposited on the ridge of an edge-emitting laser has been designed and fabricated. This palladium film is well known to react to hydrogen, forming palladium hydride with optical properties dependent on the hydrogen concentration. This reaction yields a change in complex refractive index and thus also the laser's output power. The advantages of these sensors are their small size, high sensitivity, wide dynamic range, inline integration, and scalability to arrays. These capabilities surpass most traditional optical sensors, which generally utilize fiber gratings, surface plasmon resonances, or surface reflectance. Although those methods can be effective, the edge-emitting laser sensors are easier to miniaturize, integrate, and array.

This thesis is organized into four sections. First, a brief analysis of the rising importance of hydrogen energy sources and various hydrogen sensing mechanisms is presented, followed by an overview of the edge-emitting laser sensor in terms of device design and physical sensing properties. A detailed description of the associated fabrication process is given, along with its test setup. Finally, the device performance with regards to varying concentrations of hydrogen is analyzed, with suggestions for future work and improvements.

Acknowledgments

I am grateful for the help of my adviser, Professor Lynford Goddard for his support and guidance throughout the process of my designing, fabricating, and characterizing these devices. Additionally, I would like to acknowledge the efforts of the rest of the Photonic Systems Laboratory for all of their support and advice. Without their help, I could not have accomplished this project.

Additionally, I would like to thank my family for their support and encouragement through all of my academic endeavors. None of this would have been possible without them.

Table of Contents

Chapter 1: Introduction

1.1 Motivation

Since the Industrial Revolution, fossil fuels have been used extensively to pave the way for new innovations in transportation and technology. However, due to tremendous economic growth and a rising world population, fossil fuels are being consumed in unprecedented quantities. Although they have been able to meet the world's demand for energy today, their nonrenewable nature will inevitably lead to a worldwide shortage in the foreseeable future. Additionally, the combustion products from these materials are responsible for numerous environmental threats, including pollution, acid rain, and the depletion of our ozone layer. The comfortable quality of life we take for granted today is in jeopardy, and in order to protect it, something radical must be done.

Due to this ever-increasing demand for newer technologies, alternative fuel sources must be developed to step up and eliminate our dependence on fossil fuels. Many options are being developed, including thermonuclear energy, nuclear breeders, solar energy, wind energy, hydropower, geothermal energy, ocean currents, tides, and waves. All of these are feasible alternatives for efficient electricity production, but none can truly be used directly as fuel, which is particularly important for transportation applications. Possible candidates for fuel alternatives currently being researched include synthetic gasoline, synthetic natural gas, methanol, ethanol, and hydrogen. Of these alternative fuels, hydrogen stands apart from the rest due to its virtually unlimited quantity, versatile nature, significantly higher efficiency when being converted into a desired form of energy, and ability to be used without producing pollutants. In fact, from these properties, it can be said that hydrogen is the best possible fuel being developed today [1].

A major concern when investigating novel technologies is the safety impact on both developers and consumers. The most commonly recognized potential safety hazards of newly researched fuels are the toxicity of the fuel and its byproducts, and its flammability. Hydrogen itself does not present any toxicity concerns, and when burnt with oxygen, the only exhaust is water vapor. However, when burnt with air, lean mixtures must be used to avoid the formation of nitrogen oxides, which are similar to the byproducts from currently used fossil fuels. Due to its ability to prevent the formation of nitrogen oxides when used, hydrogen is considered a relatively safe material in terms of toxicity. However, the primary safety concern that still stands in the way of mass production and public adoption is a low explosive limit of hydrogen concentrations, as low as 4% in air [2].

Due to the high temperature nature of most transportation systems, flammability concerns must be quelled before we can usher in a new hydrogen-based economy. Therefore, in order for hydrogen fuel cells to be feasible for transportation applications, reliable sensors with the ability to detect hydrogen leakage at very low concentrations with a quick-enough response time to prevent severe accidents are a necessity. The essential parameters (for gauging the quality of hydrogen sensors for fuel cell applications) are sensitivity to low concentrations, selectivity to hydrogen gas, fast response time, reusability and durability for long-term use, and economic scalability for mass production.

1.2 Current Research in the Field

Due to the recognized promises of hydrogen fuel cell technology, a great deal of work has been invested over the years in the development of adequate sensors to subdue safety concerns over hydrogen usage and storage. Research has been performed on various mechanisms to detect trace concentrations of hydrogen, which have been incorporated into a variety of

different types of devices. The most common devices for hydrogen detection are based primarily on either the electrical or optical parameters of specific materials known to react with hydrogen. The most commonly used reactionary materials are palladium and platinum because of their high sensitivity and selectivity to hydrogen. Due to palladium being the more economical of the two materials and possessing a higher sensitivity, it is used much more frequently.

When gaseous hydrogen molecules come in contact with palladium, some of the hydrogen atoms disassociate from their molecular state and diffuse into the metal, forming a palladium hydride. This absorption results in structural changes as the palladium, denoted as being in the α phase, gradually transitions to the palladium hydride β phase [3]. This phase transition occurs at a specific hydrogen concentration ranging from 0.1% to 2%, depending on the thickness and quality of the palladium film. The primary source of interest in the use of palladium as a hydrogen sensing agent is the fact that it is capable of absorbing up to 900 times its own volume of hydrogen [4].

During this transition, the lattice constant of the metal changes, up to a maximum of 3%, which decreases the conductance of the film as a function of hydrogen concentration. The conductance differential can be measured electrically, allowing one to easily determine the corresponding hydrogen concentration. Additionally, palladium has shown its merit in optical applications due to a change in reflectance or transmittance when exposed to hydrogen. This change is caused by an increase in the Fermi level and subsequent decrease in both the real and imaginary components of the dielectric function as the palladium forms palladium hydride. This decrease of the dielectric function results in a decrease in reflectivity as a function of hydrogen concentration [5]. Furthermore, palladium-based sensors are considered reversible because the

electrical and optical properties mostly reset back to their original values as hydrogen is allowed to escape from the film; however, frequently repeated transitions can cause some deterioration.

To demonstrate a sensor utilizing the change in contact resistance of palladium films after exposure to hydrogen, one group from the Argonne National Laboratory developed a purely resistive device for hydrogen sensing. Their work involved depositing palladium nanoparticles onto a layer of networked semiconducting single-walled carbon nanotubes (SWCNTs) on a flexible plastic substrate. Two electrodes were fabricated on each side of this functionalized film to measure changes in electrical resistance. Their devices exhibited a 2% change in resistance for hydrogen concentrations as low as 100 parts per million (ppm), and a 400% change in resistance for hydrogen concentrations as high as 1% (10,000 ppm). The response times of these chemiresistors were as low as 20 seconds. The most interesting merit of this work was the inclusion of the flexible plastic substrate, allowing for a wider variety of device geometries. Additionally, the group demonstrated higher sensing characteristics than many traditional devices using pure palladium layers on rigid substrates [6].

To take the principles of differential contact resistance further, one group from the National Cheng-Kung University in Taiwan used palladium as a contact metal in an AlGaN-based Schottky diode. In this device, hydrogen molecules diffuse into the interface between the palladium contact and the AlGaN. The built-in electric field then polarizes the hydrogen atoms to form a dipole layer. This dipole layer decreases the Schottky barrier height, changing the diode's current-voltage (I-V) characteristics. The diode breakdown voltage was found to be systematically dependent on the hydrogen concentration. These devices were capable of detecting hydrogen concentrations as low as 15.2 ppm, and had a minimum response time of 4 seconds [7]. As shown, this group's use of the properties of palladium in a more complex

electronic device allowed for improvements in both the sensitivity and response time. The downside to this particular implementation, however, is that the group recognized that the change in breakdown voltage was strongly dependent on the working temperature. Unfortunately, strong temperature dependence can create a reliability problem when implemented in transportation applications.

Another example of hydrogen sensors based on the electrical properties of palladium films was developed at the Tokyo Metropolitan University. Researchers there used palladium as the material for a gate electrode to an AlGaN/GaN high electron mobility transistor (HEMT). In their experiments, I-V measurements were performed on the devices as varying hydrogen concentrations utilizing a nitrogen carrier gas were flowed. Their results showed a change of 1.7 mA of drain current variation for a concentration of 1 ppm hydrogen. The group also predicts that a drain current variation of 1 mA can be achieved for a concentration as low as 450 parts per billion (ppb). Additionally, these devices demonstrated a transient time as low as 23 seconds [8]. These particular devices are impressive due to their exceptionally high demonstrated and predicted sensitivities. Additionally, the output current change in these sensors can be easily measured for even very small concentrations of hydrogen.

As mentioned, in addition to the electrical properties of palladium hydride, varying optical parameters can also be incorporated into a hydrogen sensor. In fact, optical sensors would have many advantages over classical electrical sensors, including utilization for remote sensing applications, use in environments with electromagnetic interferences, or use in environments with a high background hydrocarbon concentration, which would interfere with sensors based on heated, catalytically active materials. Additionally, optical sensors can be designed in such a way that the active sensing layer would have no electric circuit in contact with the hydrogen

environment, preventing potential ignitions [5]. Most optical detection techniques use measurements of the transmission or reflectance of palladium films, monitoring the optical changes by surface plasmon resonance measurements, or interferometric measurements [9].

Bévenot et al. used the effect of surface plasmon resonance (SPR) by depositing a thin layer of palladium on an optical fiber [10]. As in most sensors based on the principles of SPR, the shift in the resonance curve is based primarily on a variation of the refractive index of the dielectric medium surrounding the metallic layer. As the thin palladium film absorbs hydrogen, the complex permittivity of the layer changes, shifting the resonance. This shift in resonance is then measured by a change in the intensity of the light transmitted though the fiber. Using these techniques, this particular group's sensors are capable of detecting hydrogen concentrations as low as 0.8% within a nitrogen ambient, with response times ranging from 3 seconds to 300 seconds, depending on the concentration of hydrogen. This work successfully demonstrates the use of palladium hydride's dynamic optical properties as the foundation for an effective hydrogen sensor [10].

Villatoro et al. have recently used a similar optical technique, using a thin palladium coating on a tapered fiber [11]. In this implementation, a portion of the cladding has been stripped from the fiber, so the palladium film rests much closer to the core. In these devices, the evanescent waves of the transmitted signal interact with the palladium film. When the film comes in contact with hydrogen, the optical properties of the medium change, causing variations in the output signal from the fiber. This group's sensor is capable of detecting hydrogen concentrations as low as 0.05% (500 ppm), with a response time of 10 seconds [11]. In fact, this principle of placing a thin layer of palladium beneath the cladding, near the core of a waveguide, is a fundamental aspect of the scope of this new research.

As demonstrated, much of the leading research in hydrogen sensing technology utilizes a thin film of palladium because of its unique combination of high sensitivity, high selectivity, and acceptable affordability. Optical sensors, as mentioned, have numerous potential benefits over electrical sensors. With an effective design, optical sensors can meet or exceed the performance specifications of electrical sensors, and are much better suited to many of the applications in which hydrogen would be important.

1.3 Research Scope

The scope of this new research focuses on the fabrication, analysis, characterization, and optimization of a new type of sensor utilizing GaAs-based edge-emitting lasers. Similarly to the previous work in optical hydrogen sensors, a thin layer of palladium will be used as a functionalized layer. Here, it will be deposited on each side of the laser ridge, very close to the active region. When the sensor comes in contact with hydrogen, the optical properties of the palladium film change, causing a change in the evanescent signal propagating through the device. This will cause the internal loss seen by the laser mode to decrease. This decrease in loss increases the output power, causing an abrupt spike when the sensor comes in contact with hydrogen.

The theoretical models present in these devices are described in a previous work, along with extensive simulation results [12]. These results indicated that the suggested minimum detection limit is around 1 ppm of hydrogen in a nitrogen carrier. With electrical tuning, the dynamic range extends from 1 ppm up to 2%, limited only by the saturation of hydrogen adsorption into the palladium.

The significant parameters that affect the sensitivity and performance of these devices are the ridge width, length, and thickness of the palladium. These parameters will all be varied to optimize the performance of the sensor. Additionally, other modifications to the device can

enhance its functionality, including using etched facets rather than cleaved facets. Etched facets allow for the fabrication of in-line photodetectors, eliminating the need for tedious calibration and allowing an entire array of sensors to be controlled purely electrically.

This breed of sensor offers the potential of small size, high sensitivity, wide dynamic range, and potential in-line integration with photodetectors. Additionally, the sensors possess the possibility to be modified into sensing a variety of alternative chemical or biological agents in situ by modifying which material is used for the functionalized film. If a fabrication process were to be developed to allow for multiple films to be patterned on different devices, this would offer 2-D scalability to arrays of sensors that are functionalized to detect different agents. One chip, controlled purely electrically, could provide a report of all suspect chemical or biological agents present. All of these parameters and capabilities have the ability to meet or surpass most conventional optical sensors. The primary advantages to these edge-emitting laser sensors are their ease to miniaturize, integrate, and array.

The following chapters detail the specifics of the devices. First, an in-depth fabrication process is described. This is then followed by an overview of the testing methods employed, with a full report of all data collected from the devices. Finally, a discussion of the device performance and potential further optimizations are offered.

Chapter 2: Device Structure and Fabrication

2.1 Material Structure

The material used for these devices is a GaAs-based structure with an InGaAs quantum well that lases at 980 nm. These wafers were grown at and purchased from EpiWorks. The material's layer structure is given in Table 2.1. The target etches for all of the devices involve etching through the GaAs cap layer and through the AlGaAs upper cladding, but stopping at the GaAs upper core. This leaves a distance of 80 nm between the palladium layer that is to be deposited and the quantum well.

Layer	Layer Name	Material	Thickness (nm)	Dopant Type	Dopant Species	Dopant Concentration (cm^{-3})
7	Cap	GaAs	100	P	C	>1E19
6	Cladding	$Al_{0.8}Ga_{0.2}As$	500	P	C	3-8E17
5	Core	GaAs	80	I	-	-
4	QW	$In_{0.2}Ga_{0.8}As$	8	I	-	-
3	Core	GaAs	80	I	-	-
2	Cladding	$Al_{0.8}Ga_{0.2}As$	1000	N	Si	1E18
1	Buffer	GaAs	100	N	Si	>1E18
0	Substrate	GaAs		N		

Table 2.1 - Material Structure for Fabricated Devices

The specific device structure has gone through several design iterations since its initial conception, and has been changed to account for practical fabrication and testing methods. The initial scheme for the devices was to develop an entire chip of hydrogen sensors with a large array of varied parameters. After measurements were made, solid conclusions about the effects of each parameter could be drawn, and the optimization process for these devices would be performed. Additionally, aspects of an appropriate testing setup were considered.

2.2 Initial Layout

Since the devices required an airtight confinement during hydrogen measurements, the stipulations surrounding the chamber's design helped guide the design of the devices. Traditionally, most edge-emitting lasers are either electrically or optically pumped, and the output is measured on an external photodetector calibrated for the appropriate output wavelength. It was decided to electrically pump these devices, which is typically done using large probes that contact the laser's ridge. However, a testing setup that can accommodate these large testing probes and still remain airtight would be difficult to build, and would require a large chamber volume. This large chamber volume severely limits the speed at which the target gas can be channeled into and purged from the chamber while switching gases. It was decided that if a printed circuit board (PCB) were to be used with wire-bonds to the devices, larger probes could be attached to the surrounding pads outside of the air tight chamber and still electrically contact the devices. However, collecting the light output still remained a challenge. The solution to this was to build inline p-i-n photodetectors that would capture the output from the lasers, and induce a photocurrent that could be measured using the same PCB traces and pads. This would be reasonable to do considering the fact that a standard diode laser and p-i-n diode have a similar material structure. Additionally, since the laser ridges were to be relatively narrow, it was decided to make larger pads to probe and wire-bond, which were electrically connected to the laser ridge itself. An overview of the basic device layout is presented in Figure 2.1. The narrow strip in the

Figure 2.1 - Layout of Original Sensor

center of the device is the laser ridge, the larger rectangles that run parallel to the ridge are the contact pads with periodic interconnects to the ridge, and the isolated rectangle at the top is the photodetector. As shown, the facet of the photodetector is at a slight angle to reduce back-reflections into the laser ridge. It should be noted from this layout that the laser facet must be etched, rather than cleaved. Etching has many potential benefits over cleaved facets, including the in-line photodetector, better chip scalability, and superior control over the cavity length. Unfortunately, this would inevitably lead to poorer-quality facets, which would reduce the output power and increase the lasing threshold.

The hydrogen sensitivity is predicted to be dependent on both the lasing properties and the amount of overlap between the evanescent field of the propagating wave and the palladium film. Therefore, the initially proposed design specifications that would be studied are the laser ridge width, the cavity length, the separation between the laser facet and the photodetector, and the palladium thickness. The last of these parameters would be varied at fabrication time, while the remainder would be varied according to the layout of the lithography mask. Additionally, it was suggested to try to partially "de-functionalize" the palladium film by depositing a varied amount of oxide over portions of the film. This would create a smaller surface area for interactions between the palladium film and the hydrogen molecules to occur, which should reduce the device's sensitivity. So, another design parameter to be considered was the percentage of palladium area covered with oxide. Finally, the last design parameter was the inclusion of a multi-section saturable absorber, which involved a separately biased contact in the center of the ridge waveguide. This was considered because simulations suggested that this could lead to higher hydrogen sensitivities [12]. The ridge widths varied at 1, 1.5, 2, 2.5, 3, 3.5, 4, 5, 6, 8, and 10 μm. The cavity lengths varied at 100, 200, 300, 400, 700, and 1500 μm. The

separating distance between the laser facet and the photodetector varied at 2, 3, 4, 5, 10, and 15 μm. The percentage of coverage oxide varied at 0, 20, 40, 60, 80, and 100%. Finally, the percentage of the ridge length that made up the center saturable absorber for the multi-section devices varied at 10, 20, 40, 60, and 80% of the total ridge length. Finally, the contact pad widths were about 15 μm, varying slightly to accommodate changes in the ridge width. In total, there were 172 unique devices.

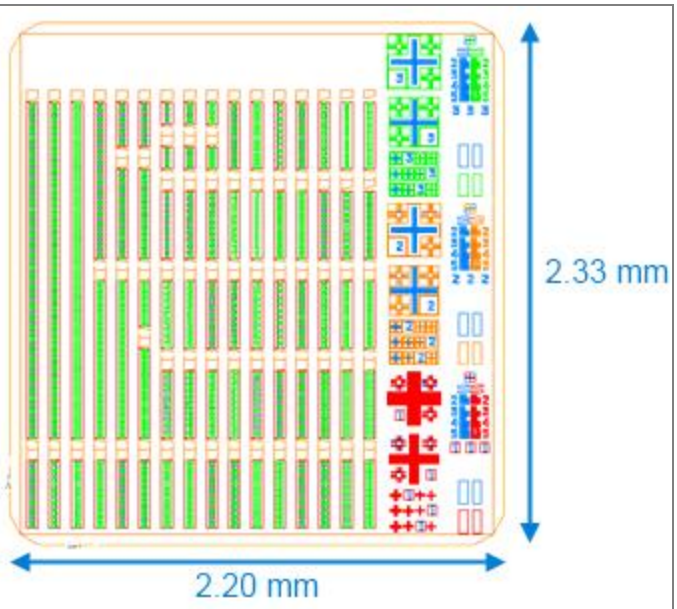

Figure 2.2 - Mask Layout of Original "Standard Die"

Since so many devices would need to be fabricated to account for the vast number of design parameters, a smaller subset consisting of 30 of these devices was chosen for a second chip that would be used for wire-bonding. Figures 2.2 and 2.3 shows layouts of the chips designed. Figure 2.2 is the standard chip that includes the full distribution of varied parameters. This chip, once fabricated, would be used in the probe station without hydrogen measurements to characterize and then fine-tune the laser performance. Figure 2.3 shows the specialized wire-

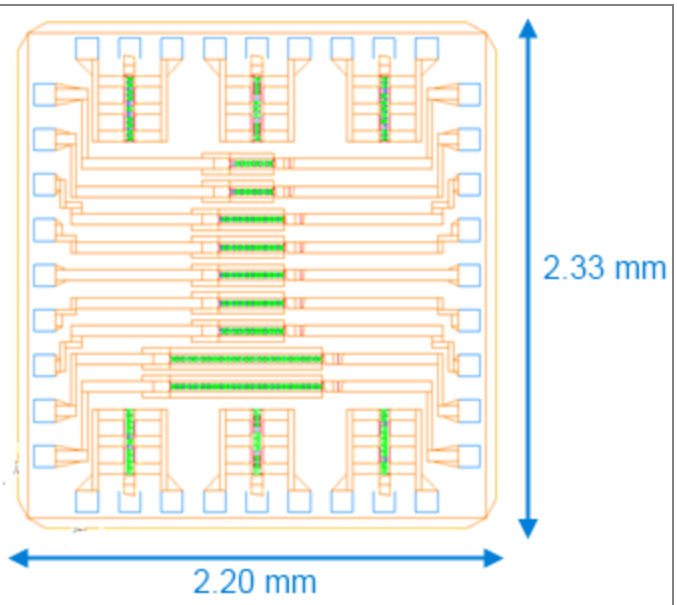

Figure 2.3 - Mask Layout of Original "Wire-bonding Die"

bonding chip that would undergo hydrogen measurements to observe how the design parameters affect the device sensitivity. It should be noted that on the wire-bonding chip, large pads (100 μm x 100 μm) surround the perimeter to serve as larger targets for the wire-bonder. The mask was designed in AutoCAD and fabricated by Compugraphics USA.

A diagram of the fabrication process is presented in Figure 2.4. The fabrication process for these devices begins with a blanket deposition of SiO_2 using a PlasmaLab plasma-enhanced chemical vapor deposition (PECVD) system. The RF power, gas flow rates, temperature, and deposition time were all set so that a 300 nm thick film would result. This oxide layer will be used as both a dry etch mask for the laser ridge, and as an insulating pad oxide to prevent current injection through the pads rather than the laser ridge. Therefore, the specific deposition parameters and film quality is negligible as long as it properly insulates current injection. The film is then patterned using photolithography with AZ5214 resist (with a 1:1 mixture of HMDS and xylene as an adhesion promoter) acting as a positive resist (portions exposed to UV light become soluble in developer). The HMDS is first spun onto the sample at 5000 rpm for 30 seconds, and then the photoresist is spun at 3000 rpm for 30 seconds. The sample then

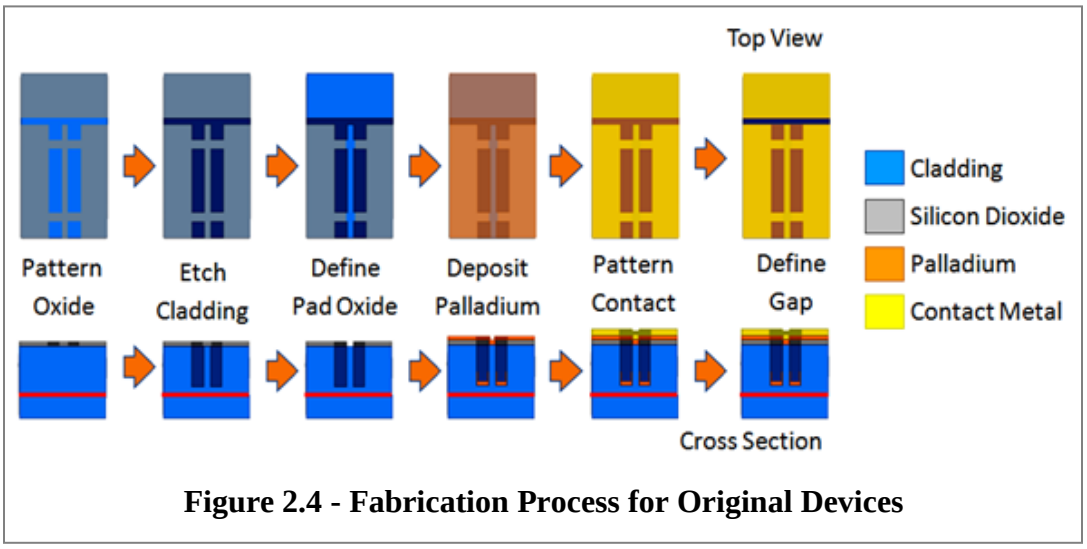

Figure 2.4 - Fabrication Process for Original Devices

undergoes a softbake procedure at 110 °C for 1 minute.

Next, the sample is placed into the contact aligner with the appropriate mask, and is exposed to UV light. This causes portions of the photoresist layer to become soluable when the sample is placed in developer. After the photolithography process is complete, the sample is inspected under a microscope to ensure the patterns resolved well. If they did not, acetone is used to remove the photoresist layer and the process is repeated. This first photolithography process is performed to define the laser ridge. The process should leave a photoresist layer about 1.6 μm thick, and serves as the basic recipe for all photolithography processes used for these devices. The sample is then placed in a PlasmaLab CF_4 (Freon) plasma reactive ion etch (RIE), which is known to etch SiO_2. This etch is performed until the SiO_2 layer has been fully etched. The patterned resist prevents etching the SiO_2 where the resist is placed, transferring the ridge pattern to the SiO_2 layer below. The resist is then removed using acetone, isopropyl alcohol (IPA), methanol, and water. Finally, the sample is descummed using an O_2 RIE process to remove any remaining traces of photoresist. The remaining patterned SiO_2 layer serves as an etch mask for the $SiCl_4$ plasma etch in a PlasmaTherm inductively coupled plasma (ICP) system known to etch both GaAs and AlGaAs.

The total etch depth is targeted at 600 nm, which should go through the GaAs contact layer, and the AlGaAs upper cladding. The bottom of the etched trench would be situated at the surface of the GaAs upper core. This is performed by starting a small etch in the material and observing the etch depth in the SEM to determine the etch rate of the tool. Additionally, several process parameters in the ICP etch are varied to witness their impact on the quality of the sidewall roughness and etch angle. Whichever process parameters produce the best-looking sample under SEM inspection are used for the remainder of the etch. After the cladding etch is

complete, the remaining SiO_2 would be used as the pad oxide; however, it had to be patterned once again to remove the oxide from the laser ridge and the photodetector contact. Therefore, the same photolithography process is performed using AZ5214 as a positive resist, and the sample is placed back into the CF_4 RIE to remove the unwanted SiO_2. The photoresist is then removed using the same method as before.

Next, a blanket palladium layer (30 nm thickness) is deposited using electron-beam evaporation. This process is performed on a CHA evaporator that has capabilities for both electron-beam and thermal evaporation. The palladium film is deposited at a rate of 1.5 Å/s until the target thickness has been reached. This places the palladium layer in the trench, as designed, and on the top of laser ridge and contact pads. Afterwards, the contact metal is patterned by first performing photolithography using AZ5125 as a negative resist (the portions of resist that are exposed to UV light are not soluble in developer). This photolithography process is mostly identical to the previous process up until the exposure. After the exposure, the sample is reverse baked at 110 °C for 45 seconds. Next, the sample undergoes a "flood exposure" without a mask for 25 seconds before the sample is placed in the developer. These additions to the process both cause the polarity of the photoresist to reverse (which can be useful for various mask designs) and change the shape of the photoresist profile. Afterwards, a blanket layer of platinum and gold (10 nm and 200 nm, respectively) are deposited in the same CHA evaporator. Platinum is deposited at 1 Å/s and gold is deposited at 3 Å/s until the target thicknesses have been met. After the evaporation, the sample is placed in acetone for "liftoff." When the sample is soaked in acetone, the photoresist becomes soluble and is removed from the sample, which lifts off the unwanted gold from the surface. It should be noted that the resist profile of the positive resist forms a trapezoid shape; however, the resist profile of the negative resist forms an inverse

trapezoid shape. This inverse trapezoid facilitates the flow of the acetone, making liftoff more manageable. It is for this reason that a negative resist is preferable for liftoff processes. At this point, the contact metal on top of the laser ridge is a stack of Pd/Pt/Au. The traditional ohmic contact for p-doped GaAs is Ti/Pt/Au. In this traditional stack, the titanium serves as an adhesion layer, the platinum serves as a diffusion barrier for gold atoms, and the gold provides high conductivity and matches the appropriate work function for the p-GaAs. This new stack substitutes the titanium layer with a palladium layer, which also has good adhesion to GaAs. It has been shown in the literature that the contact quality of the palladium-based metal stack is comparable to the titanium-based stack [13].

Finally, a photolithography process using AZ5214 as a positive resist is performed to electrically isolate adjacent devices as well as to form the facets between the laser and the photodetector. The photoresist is patterned into large rectangles that cover the entire laser structure and the photodetector structure, but do not cover the portions of the sample between the laser ridge and photodetector or between adjacent devices. This is performed by first using an aqua regia solution formed by nitric acid (HNO_3) and hydrochloric acid (HCl) (1:3) to etch the unwanted palladium in these regions, while a patterned layer of photoresist protects the gold (which can also be etched in aqua regia). Then, while leaving the photoresist mask intact, a solution of phosphoric acid (H_3PO_4), hydrogen peroxide (H_2O_2), and water (H_2O) (1:1:10) is used to etch the GaAs and AlGaAs forming the facet. The exact etch depth is trivial, but must go beyond the active region of the device, preferably into the bulk sample. This concludes the top-side processing steps.

Next, the backside of the sample is lapped down to approximately 6.5 mils total thickness and polished. This is done to reduce loss through the device and facilitate cleaving into

individual chips. Finally, the device has a metal stack deposited on the bottom (n-side) using electron-beam evaporation in the CHA evaporator consisting of Ge/Au/Ni/Au (20/50/30/50 nm), and the sample is annealed for 1 minute to form the proper n-type alloy. This metal stack forms a specific alloy on the n-GaAs surface that appropriately matches the work function of the n-type material. The samples have now been fully fabricated and are ready for testing. SEM images of the fabricated devices are presented in Figure 2.5. The provided SEM measurements in Figure 2.5 are the etch depth through the sample's upper cladding (556 nm), the thickness of the deposited contact metal (251 nm), and the angle of the etched ridge (94.39°). This etch angle is close to the ideal 90° and is the result of performing a plasma "dry etch." A chemical "wet etch" will be attempted in future design iterations, and they will not possess the same etch angle because of chemical undercutting.

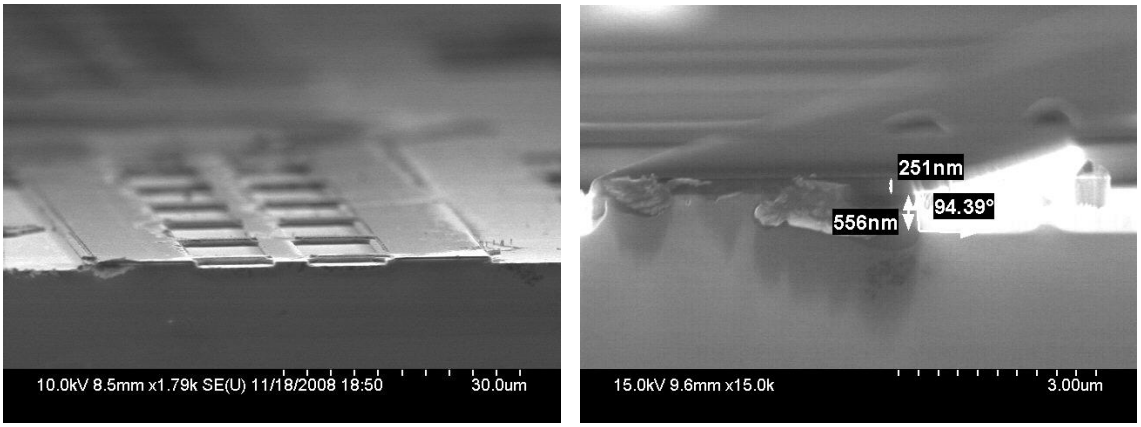

Figure 2.5 - SEM Images of the Finalized Original Devices

After these devices were completed, they underwent initial characterization. This included the generation of light output power vs. injected current (L-I) plots to determine if the finalized devices worked properly as lasers. Full details and collected data concerning these measurements are presented in a later chapter. Unfortunately, the device yield from this batch of devices was very low. Additionally, the devices that did lase, did so poorly. The threshold

currents were much higher than expected (around 400 mA), the output powers were very low (less than 3 mW), and the differential quantum efficiency was very low (about 2%).

There were a variety of identified potential causes for these problems. The first of which was the implementation of etched facets. This would greatly reduce the reflectance at each end of the cavity, which would reduce confinement, raising the threshold current and lowering the output power. Additionally, this fabrication process was very complicated in terms of the number of exact alignment steps that were needed to be made. If the contact metal was even slightly misaligned, the current would not be injected properly from the pads into the laser ridge, causing the device to fail. Additionally, the sheer number of fabrication steps and the overall complexity of the process and layout may have additionally led to device failure. At this time, the few devices that did lase were highly unreliable and as such were not worth measuring in hydrogen. The variability in each measurement without hydrogen was much larger than the expected change with hydrogen, making it impossible to detect changes as a result of hydrogen concentration. Due to the numerous potential complications, a new device layout and fabrication process was designed to help narrow down the failure sources of the devices.

2.3 Ridge-Only Layout

The second device layout that was designed possessed a much simpler structure. Instead of incorporating the contact pad layout with multiple interconnects, it used only the laser ridges. It was predicted that the probes would be able to contact these ridges if they were carefully aligned, and that the wire-bonding process might be able to stick to these ridges. Additionally, this design used cleaved facets to reduce the potential problems that can arise from the etched facets. The mask consists of parallel strips of waveguide ridges that are cleaved to define the cavity length. After cleaving, there remains a "strip" of electrically isolated devices that can then

be tested individually. A cross-section figure of the simplified devices is provided in Figure 2.6. In this iteration, it should be noted that a Ti/Pt/Au contact metal is used with the layer of palladium deposited on top of the entire contact stack. Additionally, the layout of the mask used to fabricate these devices is shown in Figure 7.

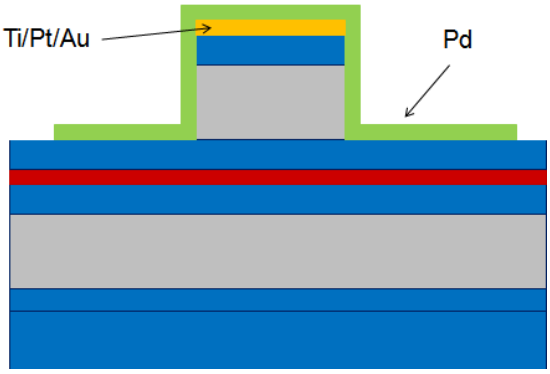

Figure 2.6 - Cross-Section of Simplified Laser Ridges

The mask was designed in AutoCAD and fabricated by the UCLA Nanolab Mask Shop. As shown, the only parameter that is varied in the mask is the ridge width. The cavity length can be varied when cleaving the devices, the palladium thickness can be varied during fabrication, and the concepts of partially de-functionalizing the palladium film and the saturable absorber have been left out for simplicity. Additionally, the variety of ridge widths has been reduced to 6 different widths, 3, 4, 5, 6, 8, and 10 µm. As shown in Figure 2.7, in between each narrow laser ridge is a wider ridge of 100 µm. This ridge serves two purposes. The first is to help dissipate pressure on the top of the sample during the backside lapping and polishing. This is done to hopefully prevent the laser ridges from getting crushed during the process. The second purpose

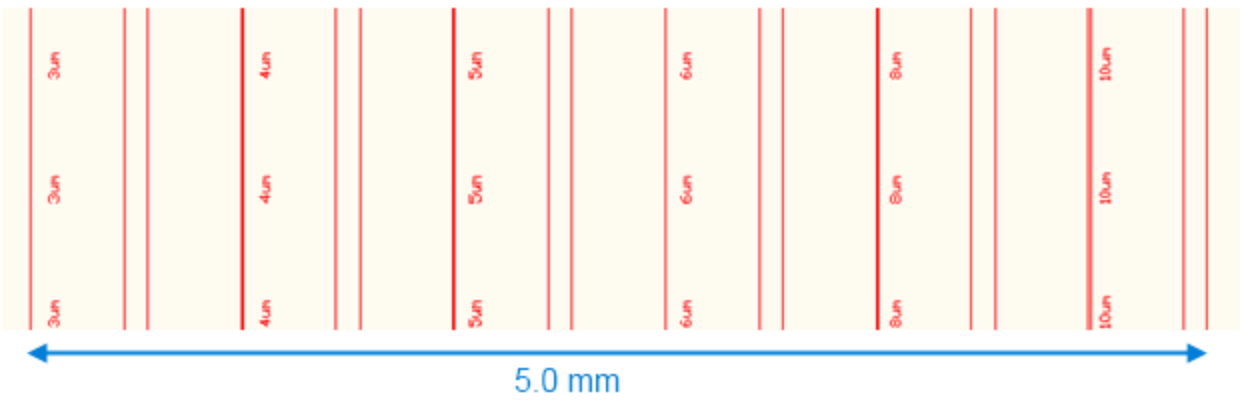

Figure 2.7 - Layout of the Narrow Laser Ridge Mask

of the wider ridges is to use them as a lithography mask for the palladium deposition. By re-using this mask shifted over to define the palladium location instead of performing a blanket deposition, adjacent devices will be electrically isolated from one another, and multiple devices can be tested on the same strip without first being cleaved individually.

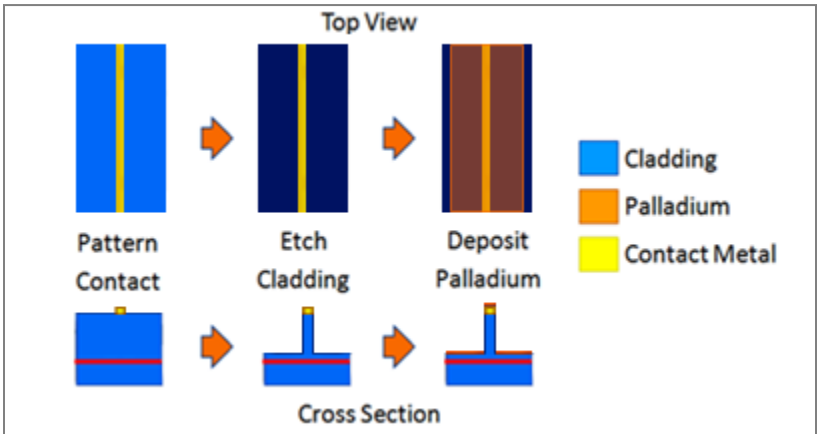

Figure 2.8 - Fabrication Process for Ridge-Only Devices

The fabrication process for these devices is much simpler. A diagram of the fabrication process is presented in Figure 2.8. It starts with patterning strips of contact metal (Ti/Pt/Au). This is done by performing photolithography using AZ5215 as a negative resist and leaving openings in the photoresist layer for the laser ridges. Then, a blanket deposition of the Ti/Pt/Au (15/10/200 nm) is performed using electron-beam evaporation. Afterwards, the sample is placed in acetone for liftoff, where the unwanted metal is removed, and all that remains on the sample are the thin metallic strips. To prevent complications from aligning the contact metal to an etched ridge, the deposited contact metal is used as a self-aligned etch mask. Unfortunately, the $SiCl_4$ plasma etch cannot be performed because using a metal mask is not recommended in the machine and also because the process will likely damage the quality of the contact metal on top

due to the constant bombardment of ions during the process. Instead, a wet etch is performed to form the laser ridges.

This wet etch process should produce smoother sidewalls; however, the large amount of undercut will prevent the etch angles from being close to the ideal 90°. The wet etch solution that was used on these devices is the same 1:1:10 mixture of H_3PO_4, H_2O_2, and H_2O that was used to form the facet on the original devices. This etch depth is controlled by etching the ridges for a few seconds, checking the etch depth on the profilometer, calculating an etch rate, and repeating. The target depth is 600 nm, to stop the etch around the interface between the upper cladding and the upper core. After this etch is complete, photolithography using AZ5214 as a negative resist is used to pattern the palladium coating (using the wide strips on the mask). Afterwards, the palladium coating (30 nm thickness) is deposited on the sample, and the unwanted portions of palladium are subsequently lifted off in acetone. Afterwards, the backside processing is performed including lapping, polishing, deposition of n-side contact metals, and annealing. SEM images of the fully fabricated devices are provided in Figure 2.9.

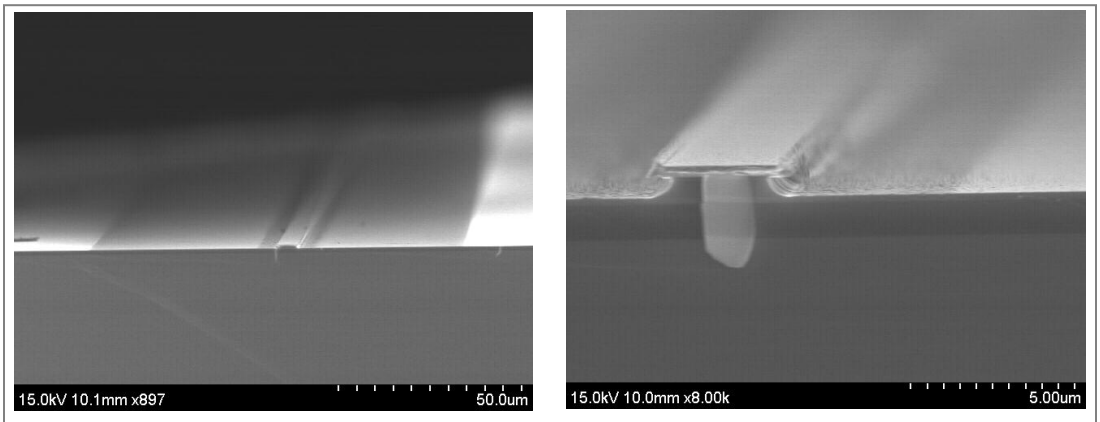

Figure 2.9 - SEM Images of Laser Ridges with Palladium Coatings

These devices underwent preliminary characterization by obtaining L-I curves to verify that the devices lased properly. Unlike the last batch of devices, most of the devices from this

batch lased properly. Additionally, the threshold currents were much lower, varying between 15 and 25 mA. Finally, the differential quantum efficiencies of these devices were as high as 26%. Compared to the previous devices, this was a major improvement. Unfortunately, after the attempts to wire-bond these devices to the printed circuit board, they stopped lasing. Upon closer inspection, it became clear that the force of the wire-bonder crushed the laser ridges, destroying the devices. It was clear that some sort of larger pad was required for bonding.

The first attempt was to try reusing the original mask with the new process to verify that a larger pad design could make the wire-bonding possible. Unfortunately, the original mask is not properly suited for facet cleaving. It is highly suspected that the etched facets were the leading cause of problems with the first batch. Thus, it was decided to fabricate these devices using the old mask and new process, and cleave them in such a way as shown in Figure 2.10. It is evident that this produces a lot of wasted devices and a very low yield. However, if these few devices can show the first signs of lasing, they can serve as a proof of concept for a future mask.

Figure 2.10 - Cleaving Method for Proof of Concept Devices

The only difference between this fabrication process and the previous ridge-only fabrication process was the inclusion of the SiO_2 pad oxide as the very first step. After that is defined, the contact metal is deposited and lifted off. Then, the trench is etched using the same wet etchant recipe as before, and finally the palladium is deposited and patterned. After the fabrication of these devices was completed, it was confirmed that they lased both before and after the wire-bonding process. However, due to the small pads (15 μm) on the devices from the full die, the wire-bonding process was difficult, and the 100 μm ball bond shorted-out adjacent pads. This led to poor current injection into the device, so the output power was very low. However, these devices served their purpose to verify that a design similar to that of the original, combined with the simpler self-aligned fabrication process, could produce successful devices. This modification and a new mask to accompany it has become the next and current iteration of the devices.

2.4 Hybrid Layout

The current implementation involves a similar contact pad structure as the first devices; however, the contact pads are wider (100 μm) to allow for easier wire-bonding, and the device layout is designed specifically for cleaved facets. Figure 2.11 gives an overview of a strip of devices with all included ridge widths. This mask was also made in AutoCAD and fabricated by the UCLA Nanolab Mask Shop. The larger pads on the left and right

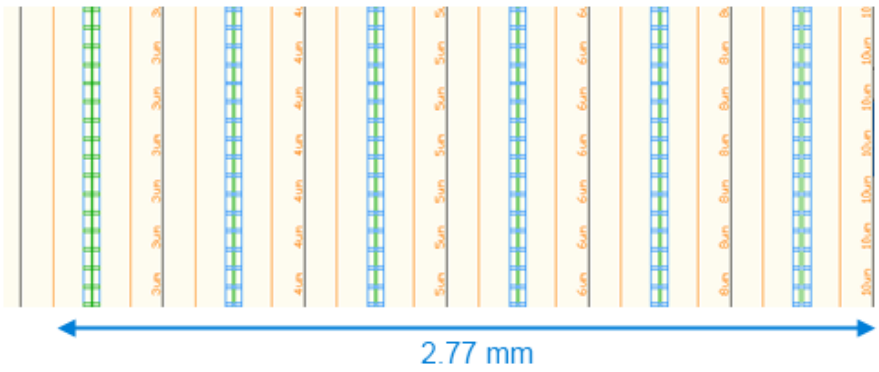

Figure 2.11 - Device Layout of a Strip of Sensors

of each device are the contact pads. After fabrication, all of these devices become electrically isolated from one another.

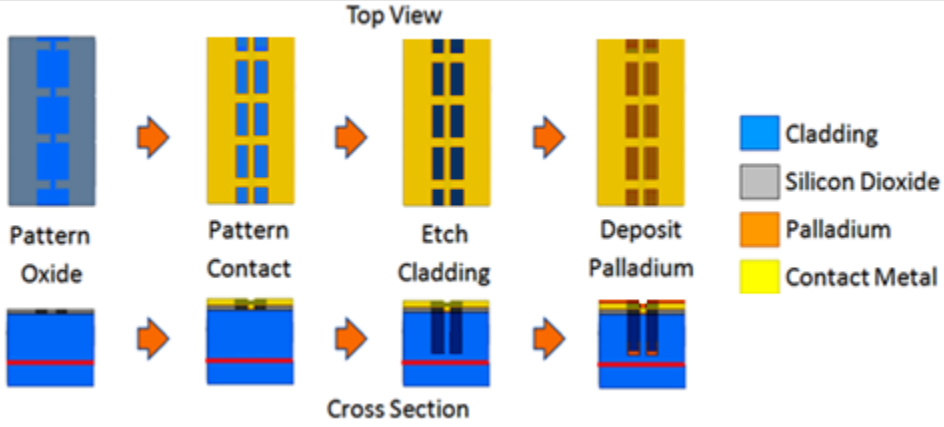

Figure 2.12 - Fabrication Process for the Hybrid Devices

The most recent fabrication procedure can be seen in Figure 2.12. It begins with a deposition of a layer of SiO_2 on the sample by PECVD. This is then patterned using photolithography with AZ5214 as a positive resist and etch using a CF_4 plasma. This film is used as insulating material for the contact pads to force current injection to occur only within the laser ridge. Next, photolithography is performed using AZ5214 as a negative resist to define the location of the contact metal. Then, the p-side Ti/Pt/Au (15/10/200 nm) contact is deposited, and then the unwanted metal is lifted off in acetone. This patterned metal contact acts as a self-aligned wet etch mask for the ridges. A H_3PO_4:H_2O_2:H_2O (1:1:10) mixture is used as the wet etchant. It is known to etch both the GaAs contact layer and the AlGaAs upper cladding. The total etch depth is 600 nm, and the depth is controlled by monitoring the etch time. Finally, the patterned palladium layer (30 nm thickness) is deposited and lifted off using the same procedure as the contact metallization. As before, these devices utilize a backside contact for current injection. After the palladium layer is patterned, the sample is lapped and polished to a much thinner size

to decrease loss in the device and facilitate cleaving. After the sample is thinned, the backside n-type contacts Ge/Au/Ni/Au (20/50/30/50 nm) are deposited, and the sample is annealed to alloy the n-type contacts. After all processing is complete, laser facets are carefully cleaved. This cleaving allows for control of the waveguide ridge length. Small "strips" of devices are obtained, each of which contain six devices of different ridge widths. The SEM images in Figure 2.13 show some of the finalized devices.

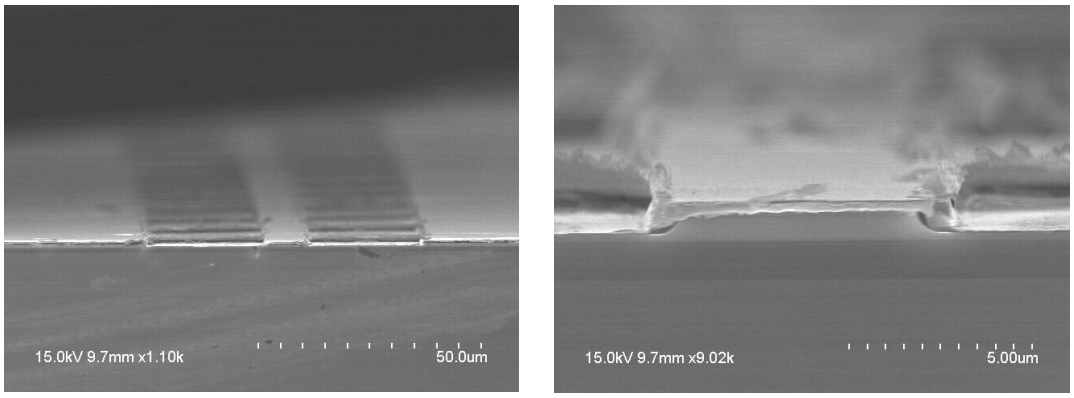

Figure 2.13 - SEM Images of Palladium-Coated Laser Ridges with Contact Pads

Chapter 3: Testing Setup and Procedures

3.1 Testing Procedure

The initial measurements for all devices were performed by using probes to inject current into the specified contact pads. For the devices with large contact pads running on each side of the ridge, one probe was placed on each contact pad, and for the ridge-only devices, two probes were placed along the length of the ridge. The testing stage is a large temperature-controlled copper block that is connected to the ground of the injected current signal. Current flows from the contacts on the top of the sample, through the laser diode, and out into the copper testing stage. The current pumped into the device is from an ILX pulsed current source with a pulse width of 1 μs. At the edge of the copper stage is a series of photodetectors. The photodetector used for these measurements is an InGaAs-based detector attached to an integrating sphere. The voltage and current measurements from the ILX pulsed current source as well as the output voltage from the InGaAs photodetector are sent to a nearby oscilloscope. A custom-made LabVIEW program controls the current source and generates current-voltage (I-V) and light output power vs. current (L-I) curves based on the signals sent to the oscilloscope.

All device types were measured using this method, including the original devices that were designed to use an integrated photodetector. The light incident on the external photodetector from the original devices is the diffracted light from the laser beam, rather than the light that was designed to enter the integrated photodetector. Therefore, the data collected for these devices presents a reliable value for the threshold current; however, the values for the output power and differential quantum efficiency are unreliable. Further measurements with the photodetector were not pursued due to the very low yield, high threshold current, and unreliability between measurements.

The hydrogen-sensing measurements needed to be taken in a custom-machined airtight chamber. Because the newer devices do not have an integrated photodetector for all-electrical operation, the measurements had to be taken with an external, InGaAs photodetector attached to an integrating sphere. For these measurements to be taken, the chamber needed either to be transparent to light at 980 nm or have a window for the output light to pass through. It was chosen to use a transparent material for the chamber, and a detailed description of the chamber design and machining process is presented in the next section. These measurements were taken by first attaching current probes to the outer pads of a printed circuit board (which makes electrical contact to the devices under test). Next, a LabVIEW code is used to pump varying levels of current through the device, while the light output power is measured on the external photodetector. While these measurements are being made, various concentrations of hydrogen gas in a nitrogen ambient are flowing through the chamber. The response of the laser's output power in relation to the hydrogen gas concentration is then recorded and used to verify the sensor's performance.

3.2 Gas Testing Chamber

The test chamber that has been designed and machined consists of a polycarbonate piece that surrounds the sample and allows gas to flow through, a printed circuit board to solder and wire-bond the sample and probe using contact pads located outside of the chamber, and a copper temperature modulation stage. The sample is first soldered onto a small copper submount using a high-temperature solder capable of withstanding the necessary wire-bonding temperatures. Then, this submount is soldered to the center of the printed circuit board. Surrounding the sample are several small pads that, via backside traces, connect to larger pads surrounding the perimeter of the printed circuit board. The proper contacts on the device to be tested are wire-

bonded to these smaller pads. Next, a polycarbonate piece with a hollowed-out cylindrical chamber is placed over the sample, and connects to the copper temperature modulation stage placed below the printed circuit board. The polycarbonate piece has a gas line running through the center of the chamber, allowing for various gas mixtures to flow over the sample. An external detector is placed outside of the chamber to collect light from the device.

Polycarbonate was chosen for the testing chamber due to its 90% transmission of visible and infrared light through 3 mm of material. This allows for accurate measurements by external detectors located outside of the chamber. Additionally, this allows for the testing of VCSELs through the transparent top. The polycarbonate piece itself is 22 x 65 mm. The cylindrical chamber has a diameter of 10 mm and a height of 7 mm. The thickness of the chamber sidewalls is 6 mm, and the thickness of the chamber top is 2 mm. The gas line running through the chamber has an 1/8″ diameter that is tapered out to an NPT 1/8″-27 pipe thread to match the 1/8″ diameter of the gas lines leading to the test setup. Photographs of the machined chamber are given in Figure 3.1.

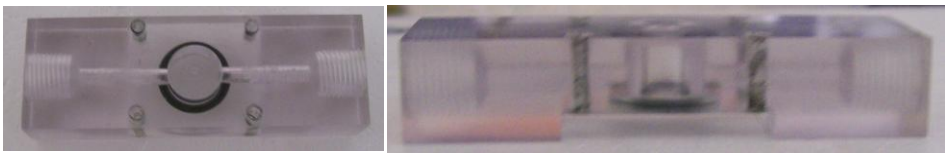

Figure 3.1 - Photographs of the Polycarbonate Testing Chamber

The polycarbonate chamber as well as the temperature modulation stage were both custom machined using resources from both the University of Illinois ECE Machine Shop and a milling machine available in one of the labs. The mechanical drawing for the polycarbonate chamber can be found in Figure 3.2. As mentioned, the polycarbonate piece is 22 x 65 mm. First, a piece of approximate size is cut from the raw material using a band saw, and is then

finely machined to the exact size. Next, four through holes (2-56) are drilled through the block, and will be used to connect the block to the copper stage. To hollow out the chamber area, a lathe is used rather than a mill because of the required precise centering of the chamber, and the ability to create fewer machining marks. Since light must travel through the sidewalls of the chamber, the machining marks and scratches must be kept to a minimum to increase the optical transmission. To affix the polycarbonate block to the lathe, a custom-made jig is used. This jig has one cylindrical end to insert into the lathe, and the other side has a slot of the same dimensions as the polycarbonate block and four tapped holes (2-56) to make use of the holes drilled through the polycarbonate. A drill bit of approximately the same dimensions as the desired chamber diameter is attached to the lathe and is used to remove the bulk of the material. Next, a custom-made lathe cutter is then used to finely remove material from the center of the chamber until the exact dimensions of the chamber have been defined. Even though by nature, the lathe causes fewer machining marks, some are still present. The optical transmission is improved by polishing the inside of the chamber using a silicon carbide polishing compound. This is performed by running the lathe and—using a cotton swab soaked in the polishing compound—rubbing the swab up and down the sidewalls of the chamber. This noticeably cleared up much of the machining marks. Next, to form the gas line, a 1/8″ diameter through hole is drilled through the length of the polycarbonate block using the milling machine. Afterwards, a

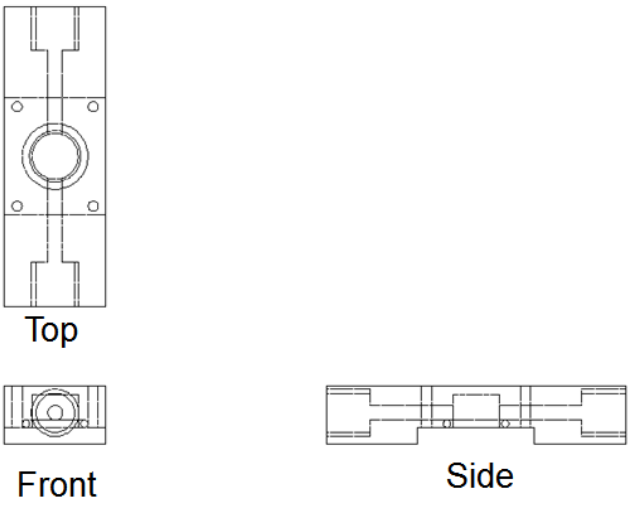

Figure 3.2 - Mechanical Drawings for Polycarbonate Testing Chamber

larger diameter portion is drilled through the center of the through line at the very edges using a size Q drill bit. This portion is then threaded using an NPT 1/8″-27 tap, which allows gas line connectors to be screwed into it. At this point, the chamber has been defined and the gas through line with threaded connectors has been formed.

The next step is to machine a slot at the bottom of the polycarbonate block into which to insert the printed circuit board. The slot width matches the printed circuit board width (25.4 mm) and is removed using the milling machine. Next, to create an airtight seal between the polycarbonate chamber and the printed circuit board, an O-ring must be used. The polycarbonate block is placed back into the lathe with the custom jig, and a wider-diameter circular shelf is removed around the opening of the chamber. The O-ring is then placed in this circular shelf. Finally, to once again promote optical transmission through the sides of the testing chamber, the polycarbonate is polished. This time it is performed using varying grades of sandpaper and rubbing the polycarbonate sides against them.

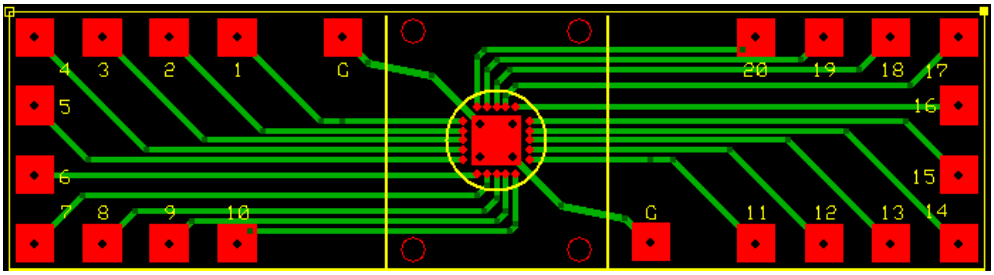

Figure 3.3 - Design Layout of the Printed Circuit Board

The printed circuit board was fabricated by ExpressPCB and designed using their software. The printed circuit board design is shown in Figure 3.3, and a photograph of the top surface of the fabricated board is shown in Figure 3.4. The pads in red are the copper pads that appear on the top surface of the printed circuit board, the green lines are traces that appear on the bottom side, and the yellow text is the silkscreen mask used for labelling the pads. It has a 5 x 5

mm square in the center in which to solder the devices. Surrounding this square are 20 round pads of 787.4 µm diameter. Each of these connects to a 3.8 x 3.8 mm square pad via backside traces.

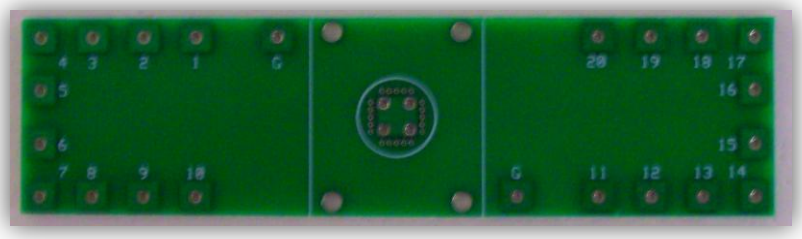

Figure 3.4 - Photograph of the Top Surface of the Printed Circuit Board

The wire-bonding process can be difficult, and it has taken time to perfect a procedure that is readily repeatable. While working on this, a variety of solder methods and wire-bonding parameters and techniques have been investigated. The solder process that was finally settled on is to first use Indalloy #204 solder to adhere the sample to a copper submount. This solder is 70% In and 30% Pb, and melts at 175 °C. The bonding is performed by first heating up the copper submount to 175 °C using a hotplate, and then placing a piece of the solder on it to melt. After the solder melts, it is spread over the surface of the copper submount using a razorblade to produce a thin, uniform layer. The sample is then carefully placed on the melted solder layer, taking care not to let the solder rise up and cover the laser facets. Afterwards, the copper submount is removed from the hotplate and pressure is applied to the surface of the sample until the solder hardens. Then, Indalloy #2, which is 80% In, 15% Pb, and 5% Ag, and melts at 154 °C, is used to adhere the copper submount to the printed circuit board. This is performed using the same method. First, the printed circuit board is heated up to 154 °C, and then a piece of solder is placed on the surface. A razorblade is used to spread this melted solder layer, and the

copper submount is carefully placed onto the solder and pressure is applied until the solder hardens. Afterwards, a thin layer of Arctic Silver Alumina is spread over the portions of the copper submount not containing the sample. This provides an electrically insulating (though not temperature insulating) layer to produce shorts between the wire-bonds and the copper submount. Finally, the printed circuit board is loaded into the wire-bonding machine and heated to 125 °C. The bonds are formed by first bringing a probe containing a thin gold wire down on one of the device pads. The heated sample helps melt the gold ball at the tip of probe until the gold wire is properly bonded to the sample. Next, the probe is carefully moved to one of the surrounding pads on the printed circuit board. A wedge bond is formed on this pad by forcefully bringing the gold wire down on the pad and scraping it against the pad. If the process is successful, the gold wire is bonded to both the device contact pad and the printed circuit board contact pad.

The temperature modulation stage consists of two copper blocks with a Peltier TEC sandwiched between them. A hole is drilled through the center of the top smaller block on a side face, and a thermistor is inserted. Connections from the TEC and the thermistor are attached to a PID controller built into one of the ILX Lightwave laser sources to help regulate the temperature of the sample. Photographs of the machined temperature modulation stage are given in Figure 3.5.

Figure 3.5 - Photographs of the Temperature Modulation Stage

The mechanical drawings for the temperature modulation stage can be found in Figure 3.6. Like the polycarbonate chamber, both blocks are first cut to approximate sizes using a band saw, and are then finely machined to the exact sizes. The smaller (top) block is 25.4 x 25.4 mm while the larger (bottom) copper block is 25.4 x 60 mm. Next, four holes (2-56) are drilled into the smaller copper block to allow connection to the polycarbonate chamber. Unlike the chamber's holes, these four holes are then threaded using a 2-56 tap. Next, three through holes are drilled into the smaller copper block to allow connection to the larger copper block. Finally, a hole is drilled from the side of the smaller copper block to the center of the block (not going completely through the width of the block), and a thermistor is placed inside using a non-electrically-conductive thermal compound. The larger copper block then has three holes drilled into it to allow attachment to the smaller copper block. However, these holes are threaded using a 2-56 tap. Now, a Peltier TEC is sandwiched between the blocks and bonded to each of them with a thin layer of silver print. To further secure the blocks, plastic screws are placed through the three through holes in the smaller block into the threaded holes in the larger block. Finally, the leads from both the thermistor and the TEC are soldered to a cable that is then plugged into the temperature controller.

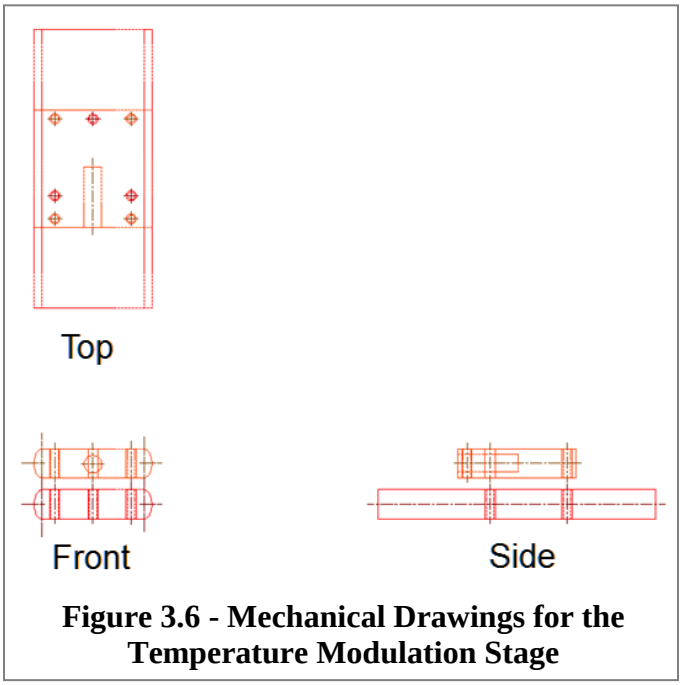

Figure 3.6 - Mechanical Drawings for the Temperature Modulation Stage

Finally, the chamber is assembled. First, the printed circuit board is sandwiched between the polycarbonate chamber and the temperature modulation stage in the slot formed in the polycarbonate. Next, four 2-56 screws go through the holes in the polycarbonate block and printed circuit board and screw into the threaded holes on the upper block of the temperature modulation stage. Finally, plastic barb connectors with an NPT 1/8″-27 connector are screwed into the threaded holes in the polycarbonate block. The appropriate gas line is now connected to these barbs, and measurements can be made. The final mechanical drawing of the fully assembled chamber is given in Figure 3.7.

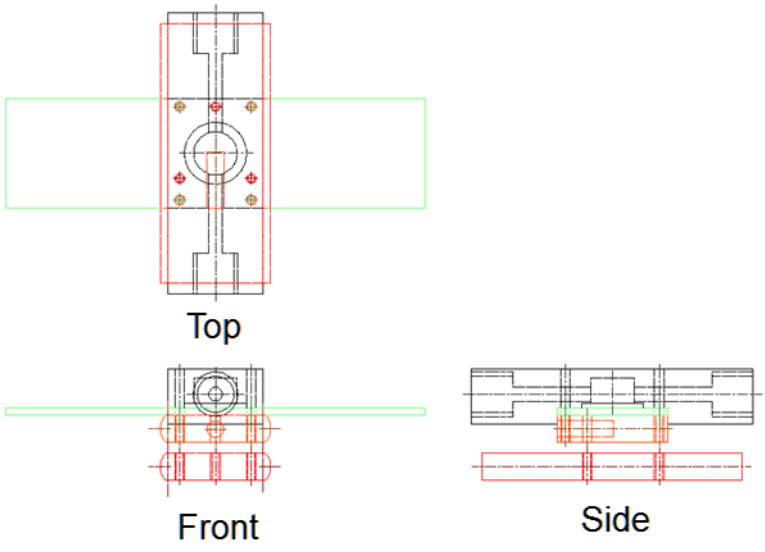

Figure 3.7 - Mechanical Drawings of the Fully-Assembled Gas Chamber

3.3 Gas Flow System

The gas flow system was designed to quickly switch between the gases to be measured. The system works by sending a gas mixture to the input of the test chamber, and the exhaust of the gas chamber is sent to the lab's dump line. The gases to be sent into the chamber are hydrogen diluted with nitrogen and pure nitrogen. For the input gas mixture, there is a mass flow controller (MFC) for the nitrogen flow and an MFC for the hydrogen flow. Since the switching time for the MFCs can take longer than desired, an electrically operated solenoid valve with a response time of 20 to 30 ms is used to switch between gases. During operation, the mass

flow controllers are on, and nitrogen is flowing into the chamber. Without applying an electrical bias to the solenoid valve, the hydrogen from the mass flow controller is sent directly to the dump. When a voltage is applied to the solenoid valve, the hydrogen is mixed with the nitrogen and sent to the input of the chamber. Additionally, there is a second nitrogen mass flow controller continuously sending nitrogen to the dump. This is to dilute the dumped hydrogen in the lines for safety purposes. In the future, additional test setups for different types of devices will be made, and a variety of other trace gases will be added. Each new trace gas will require a mass flow controller and a solenoid valve, and will connect to the current hydrogen flow system. Additionally, future alternative testing stations can be used by switching a series of manual valves that control which station the gases are sent to. Future gases to be added include CO, O_2, CO_2, CH_4, NO_2, and air (as an alternative carrier gas). All MFCs and solenoid valves are controlled using an Adlink PCI-6208V DAQ card and custom-made LabVIEW code.

Chapter 4: Results and Discussion

For the initial batch of devices, preliminary I-V and L-I curves were generated by injecting current through the contact pads. Due to the very low yield and relatively poor performance, photocurrents were not measured from the inline photodetectors. The L-I results shown were collected from the divergent light from the laser facet and collected using an integrating sphere. Since the results of these devices were mostly inconsistent and could not be effectively compared, only sample curves for examples of device operation are presented. Figures 4.1 and 4.2 show the I-V and L-I curves, respectively, of one of the working devices. This particular device had a ridge width of 6 µm, a ridge length of 300 µm, a threshold current of 404.89 mA, a threshold current density of 14.46 kA/cm^2, and a differential quantum efficiency of 2.3%. Most of the other devices that worked had similar parameters, with threshold currents between 350 and 450 mA. Out of all of the devices that were fabricated, the only ones that lased had ridge widths

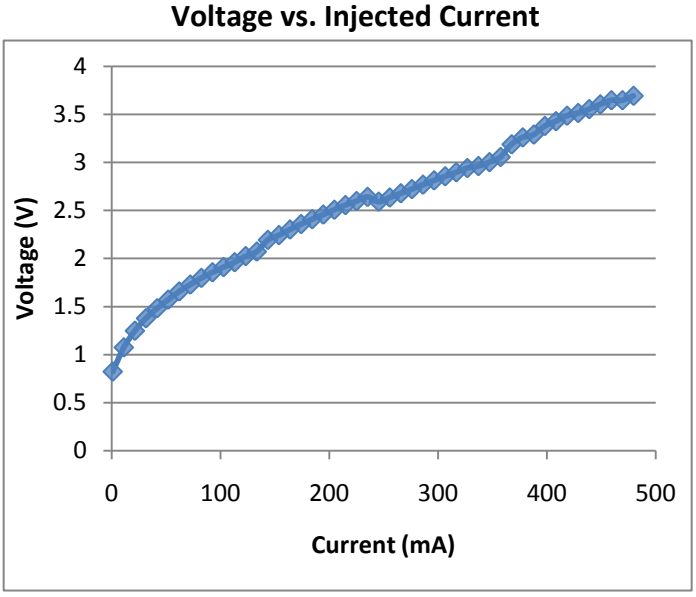

Figure 4.1 - I-V Curve for One of the Original Devices (6 µm Width, 300 µm Length)

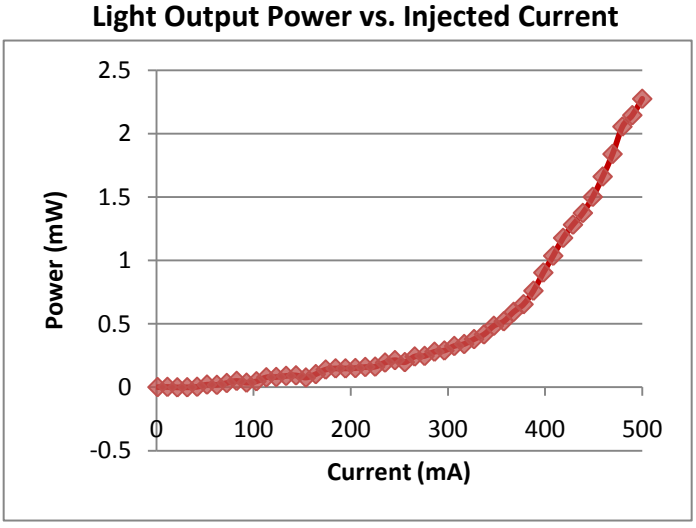

Figure 4.2 - L-I Curve for One of the Original Devices (6 µm Width, 300 µm Length)

of 4 or 6 μm. It is suspected that some of the other devices might lase at higher currents; however, the contact pads tended to burn up at about 500 to 600 mA, rendering the devices unable to be tested. The results shown in Figures 4.1 and 4.2 demonstrate that the devices acted sufficiently as diodes (see proper I-V curve shape in Figure 4.1); however, the devices were severely lacking in the quality of light output properties. As mentioned, the suspected sources of the poor performance are the etched facets, poor contacts, misalignments, or possibly the lossy nature of the palladium film.

The device structure for the second batch of devices was much simpler in nature, and did not suffer from many of the complications in the first batch. The L-I curves for three ridge-only devices of varying ridge width are shown in Figure 4.3. These data points were collected from several measurements, and show good reliability between measurements. Also notable is the significant decrease in the lasing threshold current, and the increase in the differential quantum efficiency.

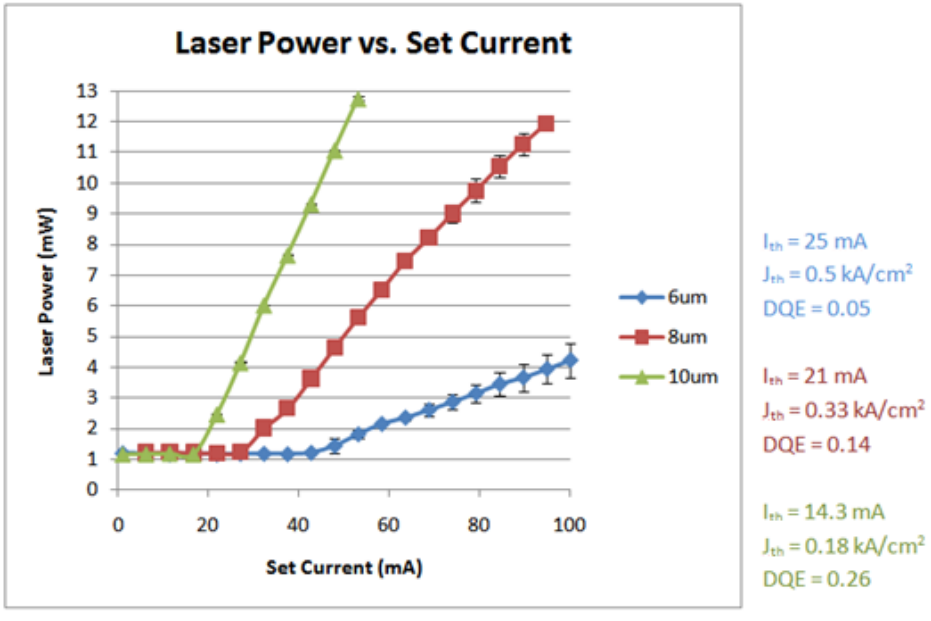

Figure 4.3 - L-I Curves for the Ridge-Only Devices

The L-I curves for various ridge widths of the third iteration hybrid devices are shown in Figure 4.4. All devices had a cavity length of approximately 1 mm (1000 µm). For the 3 µm devices, the threshold current was 47 mA, the threshold current density was 1.55 kA/cm^2, and the differential quantum efficiency was 6%. For the 4 µm devices, the threshold current was 35 mA, the threshold current density was 0.87 kA/cm^2, and the differential quantum efficiency was 9%. For the 5 µm devices, the threshold current was 32.9 mA, the threshold current density was 0.66 kA/cm^2, and the differential quantum efficiency was 14%. For the 6 µm devices, the threshold current was 39.1 mA, the threshold current density was 0.65 kA/cm^2, and the differential quantum efficiency was 18%. For the 8 µm devices, the threshold current was 25.7 mA, the threshold current density was 0.32 kA/cm^2, and the differential quantum efficiency was 24%. For the 10 µm devices, the threshold current was 36.5 mA, the threshold current density was 0.36 kA/cm^2, and the differential quantum efficiency was 19%. It should be noted from these measurements that the threshold current density decreases consistently as the ridge width is increased (with the 8 µm devices being an exception). This behavior matches that found in the ridge-only devices. However, unlike the ridge-only devices, the differential quantum efficiency seems to decrease as the ridge width is increased.

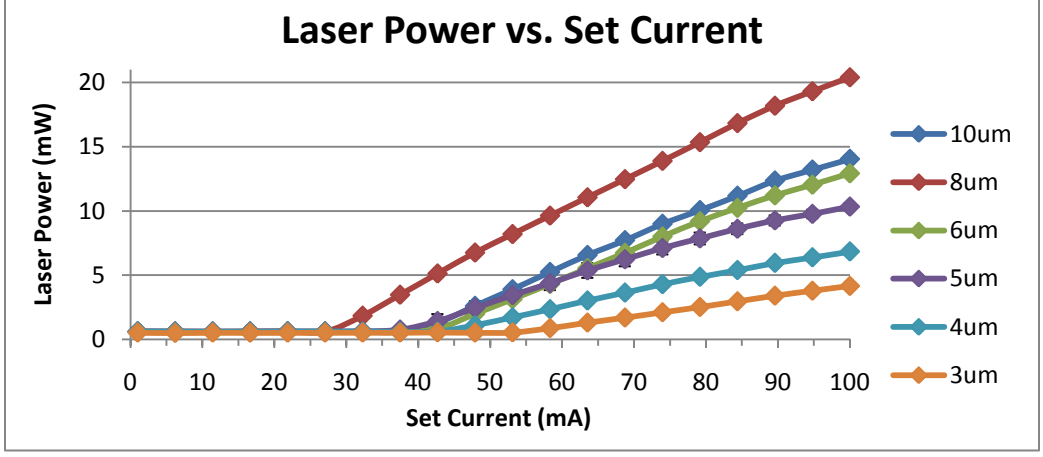

Figure 4.4 - L-I Curves for the Hybrid Devices

These changes to the threshold current density and quantum efficiency as a function of the ridge width are likely to be the result of interactions with the palladium film. As the ridge width decreases, more of the field overlaps the palladium, producing different lasing properties. One of these hybrid devices was chosen to solder and wire-bond to a printed circuit board to be placed in the gas testing chamber. The results of the hydrogen measurements are provided in Figure 4.5.

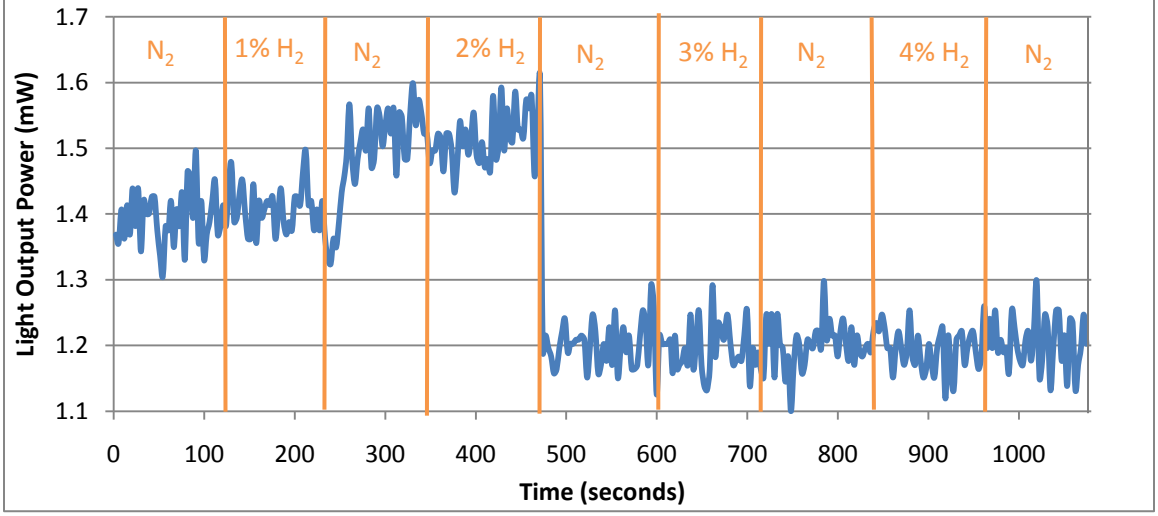

Figure 4.5 – Light Output of the Devices Over Time in Varying Hydrogen Concentrations

The results for the light output as a function of time for varying hydrogen concentrations effectively demonstrate that the presence of hydrogen makes an impact on the performance of the device. However, the achieved results conflict with the predicted theoretical operation results based on the known effects between palladium and hydrogen. The laser output power sees its greatest changes when the hydrogen is switched off, rather than switched on. These peculiar performance results will be studied and optimized in future research endeavors.

Chapter 5: Conclusion and Future Work

A new type of hydrogen sensor based on an edge-emitting laser and a palladium thin film has been presented. The device structure and design has undergone a variety of modifications to make the fabrication process and the testing procedure feasible. Both preliminary lasing properties and basic hydrogen measurements have been presented. The testing setup, including the gas flow control and the testing chamber, has been fully machined and assembled and is ready for hydrogen measurements. Additionally, the latest batch of devices that should be fully compatible with the testing station has been completed, and is shown to lase at acceptable levels of current injection. Future work will be to begin performing measurements of laser output power when varying levels of hydrogen are added to the environment.

The next stages of development will concern device enhancement and optimization. After the preliminary measurements have been taken, an analysis on devices with varying waveguide lengths will be performed to determine how the device length affects the detection sensitivity. The next parameter to be modified for device optimization is the palladium thickness. New devices will be fabricated with a variety of palladium thickness, and the effect of thickness on sensitivity will also be measured. The final parameter of the current device structure to be varied is the etch depth, which controls the amount of overlap between the palladium layer and the evanescent field of the propagating wave.

After the optimization process has been completed, a variety of device enhancements will be studied to improve the device structure and enable new functionality. The current mask has been designed to allow easy alignment to an electron-beam lithography mask, and to allow for future smaller resolution modifications to the device structure. One modification in particular involves etching an apodized grating at the edge of the waveguide, which would then be covered

with a palladium layer. This would cause the output wavelength to shift in reaction to hydrogen concentration as well as the output power. Another feature of the current mask allows a return to the integrated photodetector design to allow for full electrical operation, eliminating the need for an external photodetector. This also requires developing a new fabrication process utilizing a plasma etch to improve the facet quality between the laser and the photodetector to reduce threshold current and loss. The next direction involves replacing the palladium layer with a variety of other materials that are known to be sensitive to gases other than hydrogen, and testing the devices' sensitivities to these gases as well as their cross-sensitivities to non-target gases. Finally, the ultimate goal of this research is to design and fabricate an electrically operated full-chip design containing multiplexed gas sensors that are capable of independently sensing the concentrations of several gas species simultaneously.

References

[1] T. N. Veziroğlu and S. Şahin, "21st Century's energy: hydrogen energy system," *Energy Conversion and Management*, vol. 49, pp. 1820-1831, February 2008.

[2] L. Schlapbach and A. Züttel, "Hydrogen-storage materials for mobile applications," *Nature*, vol. 414, pp. 353-358, November 2001.

[3] T. B. Flanagan and W. A. Oates, "The palladium-hydrogen system," *Annual Review of Material Science,* vol. 21, pp. 269-304, 1991.

[4] A. Othonos, K. Kalli, and D. P. Tsai, "Optically thin palladium films on silicon-based substrates and nanostructure formation: effects of hydrogen," *Applied Surface Science*, vol. 161, pp. 54-60, January 2000.

[5] Z. Zhao, M. A. Carpenter, H. Xia, and D. Welch, "All-optical hydrogen sensors based on a high alloy content palladium thin film," *Sensors and Actuators B,* vol. 113, pp. 532-538, May 2005.

[6] Y. Sun, H. H. Wang, and M. Xia, "Single-walled carbon nanotubes modified with Pd nanoparticles for high-performance, flexible hydrogen sensors," *Journal of Physical Chemistry*, vol. 112, pp. 1250-1259, October 2007.

[7] T. H. Tsai, et al., "Comprehensive study on hydrogen sensing properties of a Pd-AlGaN-based Schottky diode," *International Journal of Hydrogen Energy*, vol. 33, pp. 2986-2992, May 2008.

[8] S. Nakamura, N. Takahashi, and T. Okumura, "Detection of ppm-order hydrogen gas by Pd/AlGaN/GaN high electron mobility transistor-based sensors," *Phys. Status Solidi C,* vol. S2, pp. S1053-S1055, January 2009.

[9] P. Fedtke, et al., "Hydrogen sensor based on optical and electrical switching," *Sensors and Actuators B,* vol. 100, pp. 151-157, February 2004.

[10] X. Bévenot, et al., "Surface plasmon resonance hydrogen sensor using an optical fibre," *Measurement Science and Technology*, vol. 13, pp. 118-124, 2002.

[11] J. Villatoro and D. Monzón-Hernández, "Fast detection of hydrogen with nano fiber tapers coated with ultra thin palladium layers," *Optics Express,* vol. 13, no. 13 pp. 5087-5092, June 2005.

[12] L. L. Goddard, T. C. Bond, G. D. Cole, and E. M. Behymer, "Functionalized lateral surface coated lasers for chem-bio detection," in *Proceedings of the IEEE Sensors Conference,* 2007, pp. 1181-1184.

[13] J. H. Jang, H. K. Cho, J. W. Bae, I. Adesida, N. Pan, “Comparative studies on low-resistance Pd-based ohmic contacts on p-GaAsSb,” *Journal of the Electrochemical Society*, pp. H389-H392, 2007.